Actin crosslinker competition and sorting drive emergent GUV size-dependent actin network architecture

Yashar Bashirzadeh[1], Steven A. Redford[2,3], Chatipat Lorpaiboon[4], Alessandro Groaz[1,*], Thomas Litschel[5], Petra Schwille[5], Glen M. Hocky[6], Aaron R. Dinner[2,4], Allen P. Liu[1,7,8,9]

[1] Department of Mechanical Engineering, University of Michigan, Ann Arbor, Michigan, 48109, USA

[2] James Franck Institute, University of Chicago, Chicago, Illinois, 60637, USA

[3] The graduate program in Biophysical Sciences, University of Chicago, Chicago, Illinois, 60637, USA

[4] Department of Chemistry, University of Chicago, Chicago, Illinois, 60637, USA

[5] Department of Cellular and Molecular Biophysics, Max Planck Institute of Biochemistry, 82152, Martinsried, Germany

[6] Department of Chemistry, New York University, New York, NY, 10016, USA

[7] Department of Biomedical Engineering, University of Michigan, Ann Arbor, Michigan, 48109, USA

[8] Department of Biophysics, University of Michigan, Ann Arbor, Michigan, 48109, USA

[9] Cellular and Molecular Biology Program, University of Michigan, Ann Arbor, Michigan, 48109, USA

* Current address: Department of Neuroscience, Baylor College of Medicine, Houston, Texas, 77030, USA

Corresponding authors:

A.R.D.: dinner@uchicago.edu; 929 E 57th Street, University of Chicago, Chicago, Illinois 60637. Tel: +1 773-702-2330.

A.P.L: allenliu@umich.edu; 2350 Hayward Street, University of Michigan, Ann Arbor, Michigan 48109. Tel: +1 734-764-7719.

Abstract

The proteins that make up the actin cytoskeleton can self-assemble into a variety of structures. *In vitro* experiments and coarse-grained simulations have shown that the actin crosslinking proteins α-actinin and fascin segregate into distinct domains in single actin bundles with a molecular size-dependent competition-based mechanism. Here, by encapsulating actin, α-actinin, and fascin in giant unilamellar vesicles (GUVs), we show that physical confinement can cause these proteins to form much more complex structures, including rings and asters at GUV peripheries and centers; the prevalence of different structures depends on GUV size. Strikingly, we found that α-actinin and fascin self-sort into separate domains in the aster structures with actin bundles whose apparent stiffness depends on the ratio of the relative concentrations of α-actinin and fascin. The observed boundary-imposed effect on protein sorting may be a general mechanism for creating emergent structures in biopolymer networks with multiple crosslinkers.

The actin cytoskeleton endows cells with remarkable materials properties[1]. They can resist significant forces but also can deform to migrate through tiny spaces. The spatial organization of the cytoskeleton is critically important for coordinating the forces that enable a cell to move, change shape, and traffic molecules intracellularly[2-4]. Actin binding proteins crosslink filamentous actin (F-actin) into diverse network architectures, creating complex, heterogeneous materials in cells[5]. α-Actinin is a key actin crosslinker found in contractile units, particularly in actin stress fibers, which transmit traction forces across adherent cells[6]. α-Actinin dimers are about 35 nm long and bundle F-actin with a spacing that allows myosin binding and in turn contraction. In contrast, fascin is present predominantly at the cell leading edge in sensory protrusions such as filopodia and invadopodia[7]. There, fascin is found in tight parallel actin bundles with about 6 nm spacing. Biomimetic motility assays with branched actin networks reconstituted on polystyrene beads formed filopodia-like bundles in the shape of aster-like patterns in the presence of fascin[8, 9].

Live cell and *in vitro* studies have shown that α-actinin and fascin work together in concert to enhance cell stiffness[10]. In the presence of both α-actinin and fascin, reconstituted branched actin networks on beads formed aster-like patterns and spontaneously segregated into distinct domains: α-actinin was localized to near the surface of the beads while fascin was localized to thin star-like spikes[11]. Crosslinker size-dependent competitive binding effects of α-actinin and fascin can spontaneously drive their sorting and influence the association of other actin binding proteins[11, 12]. Theoretical models and coarse-grained simulations of two filaments bundling revealed that the energetic cost of bending F-actin to accommodate the different sizes of α-actinin and fascin was sufficient to drive their sorting into domains[13, 14].

Although biomimetic platforms such as supported lipid bilayers[15-17] and the surfaces of giant unilamellar vesicles (GUVs)[18-20] introduce appropriate boundary conditions for self-assembly of actin network components into biochemically and mechanically functional networks, they do not confine components in the way that a cell does. To address this issue, actin cytoskeletal components have been encapsulated within or attached to the interiors of lipid-coated single emulsion droplets[21-23] or GUVs[23-26]. Studies that reconstitute actin and microtubule networks from purified components have revealed that spatial confinement can change the structures formed[27-30]. Here, we investigate the emergent structures and spatial organization of actin networks crosslinked by α-actinin and fascin in a spherically confining GUV environment.

α-Actinin induces aggregation and GUV size-dependent formation of actin rings and peripheral asters.

To investigate how confinement modulates actin network architecture, we encapsulated α-actinin together with actin inside GUVs of different sizes. We 'skeletonized' *z*-stack confocal image sequences of actin (see Methods and **Supplementary Figs. S1 and S2**) to visualize and characterize actin bundles. Actin bundle architecture was found to be highly dependent on GUV size but not α-actinin/actin molar ratio **(Fig. 1a,b)**. Three types of structures were observed: single actin rings near the GUV midplane (**Supplementary Fig. S3**), distinct yet connected actin bundles with no rings (networks), or a combination of connected actin bundles and actin ring(s) around the periphery (ring/network structures). In small (7-12 µm diameter) GUVs, α-actinin-bundled actin merged into a single ring (**Fig. 1c**), similar to structures reported previously[30, 31], with high probability. The probability of finding single rings was significantly lower in medium (12-16 µm diameter) GUVs, and lower still in large (> 16 µm diameter) GUVs.

Increasing GUV size favored more complex actin network structures (**Fig. 1d**) over rings. In particular, in the majority of large GUVs, regardless of α-actinin concentration, F-actin aggregated at the GUV periphery (**Supplementary Fig. S4a, arrows)**, with large clusters proximal to the membrane (**Fig. 1e-f, Supplementary Fig. S4b-c**). We refer to these structures as 'peripheral asters' below; we also describe aster-like structures with clusters in the lumen, and we refer to them as 'central asters'. We further characterized the peripheral asters by the locations of their bundles and observed that the fraction of GUVs in which all bundles were at the GUV periphery, as opposed to in the lumen, increased with α-actinin concentration (**Fig. 1g**). The structures formed by α-actinin-actin bundles and their dependence on GUV size are summarized schematically in **Figure 1h**. Given the absence of specific binding between actin bundles and phospholipids, we interpret the preference for the periphery to result from minimization of bundle bending (i.e., elastic energy); the dependence of the bundle location on α-actinin concentration suggests that bundles span the cluster and stiffen as more crosslinkers bind. Stiffening of crossing bundles at the cluster would force actin bundle arms out resulting in the formation asters.

In contrast to the results above, the crosslinker fascin formed actin bundles that were sufficiently rigid to stably deform GUVs or were sharply kinked by the membrane as expected

(Supplementary Fig. S5)[32]. Fascin alone was unable to induce F-actin clustering or the formation of peripheral or central actin asters.

Encapsulated α-actinin and fascin together form distinct actin network architectures.

The dependence of actin network architecture on GUV size and crosslinker type motivated us to co-encapsulate α-actinin and fascin together with actin in GUVs, and we found that this resulted in the formation of additional actin structures organized around clusters **(Fig. 2a)**. These included central asters, as noted above. Actin clusters at the GUV center were always associated with an aster made up of relatively straight bundles **(Fig. 2a**, yellow arrow**)**. Clusters at the GUV periphery were associated with asters as well, with bundles that curved around the GUV periphery to form partial or complete rings **(Fig. 2a**, white arrows**)**.

Otherwise, we observed similar trends as previously **(Fig. 2b)**. **Figure 2c** schematizes typical GUV size-dependent actin network architectures formed by α-actinin and fascin. The probability of actin ring formation was reduced dramatically with increasing GUV size (**Fig. 2b-d**), and there was a tendency to form network (and ring/network) structures in medium and large GUVs **(Fig. 2e)**. The majority of the network structures in the large GUVs were asters **(Fig. 2f)**. All of these trends were insensitive to the α-actinin concentration.

While the probability of aster formation was not observed to be significantly affected by α-actinin concentration, the morphology of asters was. With increasing α-actinin concentration at a fixed concentration of fascin, the cluster in the middle of a central aster grew **(Fig. 3a**, **b)**. Compared to α-actinin-bundled actin structures, the addition of fascin significantly increased the probability of finding central asters **(Fig. 3c)**. In the presence of α-actinin and fascin, increasing GUV size also increased the probability for the cluster to be localized at the GUV center **(Fig. 3d)**. The minimization of F-actin bending energy in fascin-associated bundles together with the available space can force filaments to cross close to the center, explaining the tendency for clusters to be in the center of large GUVs. That the size of the central cluster but not the probability of forming a central aster changed with α-actinin concentration implied to us that fascin was driving bundling while α-actinin was driving central clustering. We thus investigated the distribution of the two crosslinkers within an aster.

Crosslinkers spatially sort in central asters.

Fluorescently labeled α-actinin was found to be localized to clusters in the middle of central asters **(Figure 4a-b, Supplementary Fig. S6a)**. The absence of α-actinin outside of clusters supports the hypothesis that the two crosslinkers indeed play very different roles when together **(Figure 4c, Supplementary Fig. S6a,b)**. Fascin dominates the region outside the clusters to form tightly packed straight actin bundles in a manner similar to that predicted for Arp2/3 complex-fascin-actin networks in bulk solution[33]. α-Actinin accumulates in the clusters and crosslinks the rigid bundles, which, in the absence of significant interactions with the membrane, tend to cross at the center to minimize their bending. In contrast to central asters, α-actinin was localized entirely along peripheral actin bundles, providing no evidence of spatial segregation **(Supplementary Fig. S6a, c)**.

Observing that increasing α-actinin in the presence of fascin increased the size of actin clusters in the GUV center and enhanced the exclusion of α-actinin from actin bundles in central asters, we sought to explore the relation between this exclusion and the rigidity of the actin bundles. The persistence length of actin bundles as a function of α-actinin concentration without and with fascin showed that the bending rigidity of actin bundles is larger in the presence of both crosslinkers compared to α-actinin-bundled actin, as one would expect from the properties of the crosslinkers **(Fig. 4d)**. Strikingly, the persistence length of α-actinin-fascin-actin bundles increased as we increased the molar ratio of α-actinin at a fixed fascin concentration **(Fig. 4d)**. Such an increase in bending rigidity can result from a sorting mechanism in which α-actinin stabilizes a network structure that preferentially recruits further α-actinin to the GUV center and in turn enhances bundling by fascin in the periphery. At low α-actinin concentrations, the sorting is not pronounced, and α-actinin and fascin compete to bundle actin, while, at high α-actinin concentrations, the sorting results in tightly packed fascin-actin bundles with few α-actinin defects. When α-actinin concentration was constant while varying fascin concentration, the size and density of actin clusters **(Supplementary Fig. S7a-b)** and bundle persistence length **(Supplementary Fig. S7c)** did not change. This suggests that fascin cannot bind F-actin further as fascin-actin bundles outside clusters get saturated.

To understand the microscopic origin of crosslinker sorting in GUVs we turned to coarse-grained simulations of cytoskeletal dynamics. We used the simulation package AFINES[13, 34, 35] and parameterized α-actinin as a relatively long and flexible crosslinker that had no preference for

6

filament orientation and fascin as a short and stiff crosslinker that preferentially bound parallel actin filaments (see Methods). Furthermore, they had different kinetics: fascin had a fast on rate, $k_{on} = 20 \ s^{-1}$, whereas α-actinin had a slow on rate, $k_{on} = 0.2 \ s^{-1}$. To compensate for mechanical differences and ensure similar numbers of bound crosslinkers the ratio of k_{on}/k_{off} for fascin was 40 while the same ratio for α-actinin was 4. As in the experiments, fascin in the simulations produced tight, well defined bundles, while α-actinin produced flexible bundles that were much more loosely structured **(Supplementary Fig. S8)**. To ascertain whether these physical and kinetic differences can account for the sorting seen in experiment we simulated a 1:1 ratio of the two crosslinkers starting from an initial condition in which actin filaments with fixed lengths crossed close to the center of the simulation region but were otherwise randomly distributed (see Methods). After 100 s of simulation, the α-actinin (**Fig. 4e,** cyan) predominantly occupied the center of the aster, while the fascin (**Fig. 4e,** black) dominated the bundles emanating outwards (**Supplementary Fig. S9**). To rule out possible model specificity we ran simulations with similar parameters in the package Cytosim[36] and saw similar sorting (**Supplementary Fig. S10**).

To quantify these observations, we computed the probability density functions (PDFs) of crosslinkers in the simulations. Simulations with a single crosslinker led to relatively flat PDFs (**Fig. 4f**, top). Simulations with the crosslinkers together led to α-actinin PDFs with a steep maximum at the center and fascin PDFs with a shallow minimum at the center (**Fig. 4f**, bottom). To characterize the evolution of the PDFs, we computed the Binder cumulant (see Methods) as a function of time. The Binder cumulant measures the kurtosis of an order parameter, which here is crosslinker density. Higher values correspond to more uniform distributions while lower values correspond to more sharply peaked distributions. The value of the Binder cumulant for the fascin distribution is always high. This indicates that as fascin binds it shows very little spatial preference, forming bundles that span the GUV (**Fig. 4g,** black curves). This is in sharp contrast to α-actinin which, both on its own and in conjunction with fascin, always exhibits a lower value of the Binder cumulant at the beginning of the simulation before relaxing to a steady value (**Fig. 4g,** red curves). This initially low value indicates that, unlike fascin, α-actinin has a propensity to bind in one portion of the aster, i.e., the center, thus resulting in a tighter distribution and a higher value of the Binder cumulant, and only migrates outward into the periphery after these favorable positions have begun to be taken up (**Supplementary Fig. S9**). While the Binder cumulants in the single crosslinker simulations ultimately reached similar values (**Fig. 4g,** top), when the crosslinkers were

together, fascin was able to limit the spread of α-actinin, and a gap between the Binder cumulants persisted (**Fig. 4g,** bottom). These findings confirm that competition-based crosslinker sorting can give rise to the emergent structure observed experimentally.

Outlook

This work demonstrates that confinement can have a strong effect on reconstituted actin network architectures. We observe rings and both peripheral and central asters, depending on GUV size. As there are no molecular motors in our system, mechanisms that rely on contraction to position the structures[37-39] cannot be operative. A recent simulation study showed that confined actin and crosslinkers can form rings, open bundles, irregular loops, and aggregates depending on crosslinker type and concentration, and confinement geometry[40]. Our results suggest that the positions of crosslinked actin networks can result from minimization of bundle bending as a result of membrane resistance to protrusion. Our experiments and simulations, as well as previous ones[11, 13], suggest that crosslinker sorting is a factor in determining the architecture of actin bundle networks. Although α-actinin and fascin have similar actin bundling affinities *in vitro*, α-actinin has a higher binding affinity for single filaments and forms parallel and antiparallel bundles with large spacing and mixed polarity as opposed to fascin, which forms tightly packed parallel bundles[11]. α-Actinin can also form crosslinks between bundles that are neither parallel nor antiparallel[41]. These properties enable α-actinin to form more complex structures even in bulk, including bundle clusters at high α-actinin concentrations[10, 42, 43]. In our system, fascin-bundled actin filaments intersecting and coming in close proximity at the GUV center become crosslinked by α-actinin to form a central cluster (**Fig. 4h)**. This is distinct from the convergent elongation model of how filopodia emerge from a dendritic network[44]. Similarly, the star-like actin structure with fascin-bundled actin on a bead requires nucleation of branched actin filaments[8]. Thus, our study reveals a distinct mechanism for creating an emergent actin structure from a two-crosslinker system.

In the sense that the boundary positions filaments to enable this mechanism, one can view it as driving sorting. This may be a general mechanism by which cells can select between different dynamical steady states and tune their functions as a heterogeneous material. Boundary-driven protein sorting can be exploited in a synthetic cell context to generate more diverse self-assembling

cytoskeleton structures involving multiple actin crosslinkers. Reconstitution of membrane interfaces has also revealed protein exclusion machineries mediated by protein size and binding energy for effective localization of membrane proteins[45, 46]. Thus, boundary-imposed interactions present a simple yet effective way of protein sorting in cellular processes which induce positioning and activation of proteins at specific sites enabling their localized functions.

Methods

Proteins and Reagents

Actin was either purchased from Cytoskeleton Inc, USA or purified from rabbit skeletal muscle acetone powder (Pel-Freez Biologicals) as previously described[47]. ATTO 488 actin was purchased from Hypermol Inc, Germany. α-Actinin was purchased from Cytoskeleton Inc. Fascin was either purchased from Hypermol Inc, Germany, or purified from *E. coli* as Glutathione-S-Transferase (GST) fusion protein. For purification, BL21(DE3) *E. coli* cells were transformed with pGEX-4T-3 (GE Healthcare) containing the coding sequences of fascin. Cells were grown at 37 °C while shaking at 220 rpm until the OD_{600} reached 0.5 - 0.6. Protein expression was induced with 0.1 mM IPTG and cell cultures were incubated at 24 °C for 8 h. Cells were harvested by centrifugation at 4,000 x g for 15 min and washed with PBS once. Pellets were stored at -80 °C until the day of purification. Cell pellets were resuspended in lysis buffer (20 mM K-HEPES pH 7.5, 100 mM NaCl, 1 mM EDTA, 1 mM PMSF) and ruptured by sonication. Cell lysates were centrifuged at 75,000 x g for 25 min and supernatants were loaded on a GSTrap FF 1 mL column (GE Healthcare) using an AKTA Start purification system (GE Healthcare) at a flow rate of 1 mL/min. The column was washed with 15 mL washing buffer (20 mM K-HEPES pH 7.5, 100 mM NaCl) and the proteins were eluted with 5 mL elution buffer (washing buffer + 10 mM reduced L-glutathione). Purified products were dialyzed against 1 L PBS twice for 3 h and once overnight at 4 °C. Protein concentration was calculated by UV absorption using predicted molar extinction coefficients (ExPasy) of 110,700 $M^{-1}cm^{-1}$. Proteins were concentrated with Centricon filters (Merck-Millipore) when needed and/or diluted to a final concentration of 1 mg/mL in PBS.

GUV Generation and Microscopy

0.4 mM stock mixture of lipids containing 69.9% 1,2-dioleoyl-sn-glycero-3-phosphocholine (DOPC), 30% cholesterol, and 0.1% 1,2-dioleoyl-sn-glycero-3-phosphoethanolamine-N-(lissamine rhodamine B sulfonyl) (Rhod-PE) in a 4:1 mixture of silicone oil and mineral oil was first made in a glass tube. The lipid/oil mixture could immediately be used or stored at 4 °C for a maximum of 2 days. DOPC, cholesterol, and Rhod-PE were purchased form Avanti Polar Lipids. Silicone oil and mineral oil were purchased from Sigma-Aldrich.

Next, 5 µM Actin (including 10% ATO 488 actin) in polymerization buffer (50 mM KCl, 2 mM $MgCl_2$, 0.2 mM $CaCl_2$, and 4.2 mM ATP in 15 mM Tris, pH 7.5) and 5% OptiPrep was prepared and kept in ice for 10 min. α-Actinin (0.5-1.5 µM) and/or fascin (0.5-1.5 µM) were then added to the sample. GUVs were generated in 20-30 s after the addition of crosslinkers.

GUVs were generated by a modification of the cDICE method[48] (**Supplementary Fig. S1a**). A rotor chamber was 3D-printed with Clear resin by using a Form 3 3D printer (Formlabs) and mounted on the motor of a benchtop stir plate and rotated at 1,200 rpm (60 Hz). 0.71 mL aqueous outer solution (200 mM D-glucose matching the osmolarity of inner solution) and around 5 mL of lipid-in-oil dispersion are sequentially transferred into the rotating chamber. The difference in density between the two solutions results in the formation of two distinct layers with a vertical water/oil interface at their boundary. GUV generation was initiated by introduction of 15-20 µL inner solution carrying actin and actin-binding proteins in polymerization buffer containing 5% OptiPrep through a nozzle. Alternatively, a water-in-oil emulsion was first created by vigorously pipetting 15-20 µL of actin polymerization solution (including 5% OptiPrep) in 0.7 mL of lipid/oil mixture and the emulsion was pipetted into the rotating chamber. In either case, generated droplets travel through the lipid dispersion. Lipids are adsorbed at the droplet interface to form a monolayer. As the droplets cross the vertical water/oil interface, they acquire the second leaflet of the bilayer and get released in the outer solution as GUVs (bottom panel of **Supplementary Fig. S1a**).

The outer solution containing GUVs were transferred to a 96 well plate for microscopy. The presence of OptiPrep in GUV lumen increases GUV density and helps GUVs to sediment on the bottom of well plate. Plates were imaged 1 hour after the generation of GUVs unless otherwise mentioned. Images were captured using an oil immersion 60 x/1.4 NA Plan-Apochromat objective

on an Olympus IX-81 inverted microscope equipped with a spinning disk confocal (Yokogawa CSU-X1), AOTF-controlled solid-state lasers (Andor Technology), and an iXON3 EMCCD camera (Andor Technology). Image acquisition was controlled by MetaMorph software (Molecular Devices). Actin and lipid fluorescence images were taken with 488 nm laser excitation at exposure time of 350-500 ms and 561 nm laser excitation at exposure time of 20-25 ms respectively. A Semrock 25 nm quad-band band-pass filter was used as the emission filter. Z-stack image sequence of actin and lipids were taken with a step size of 0.5 μm. It should be noted that photo-bleaching of fluorophores significantly impaired actin network self-assembly at the early stages of actin bundling in GUVs. This prevented us from capturing the dynamics of self-assembly by z-stack imaging at a high-temporal resolution.

Image Analysis

Image processing and image data analysis were performed using ImageJ/Fiji[49, 50], SOAX[51, 52], and custom MATLAB scripts **(Supplementary Fig. S2)**. All 3D images shown are maximum projections of z-tack confocal image sequences using 3D Project command in ImageJ/Fiji. For 3D characterization of actin bundle structures, we generated skeletonized models from regions of interest in actin images. In order to optimize the images for the identification of actin bundles, images were first preprocessed using Fiji (see Supplementary Methods). The structures from z-stack images are identified and extracted with SOAX source code[51, 52] by active contour methods.

SOAX program stores all the coordinates of snakes (skeletonized bundles) and joints in a .txt file. Custom MATLAB routines were written to reconstruct the text as a Chimera marker file, include a colormap for z coordinates, and save file as .cmm format. This process enabled UCSF Chimera[53] to read the file and provide a better 3D visualization of actin structures for selecting actin bundles and measuring parameters such as bundle length and radius of curvature, bond vectors, ring center of mass, and persistence length with MATLAB. GUV geometrical parameters such as diameter and membrane curvature were directly measured from lipid z-stack image sequences via ImageJ.

For more details regarding image processing and data analysis see Supplementary Methods.

Percentages and Probabilities

After taking Z-stack confocal image sequences of GUVs (561 nm) and encapsulated actin (488 nm), and image preprocessing of actin images, 3D reconstructed actin images were obtained via ImageJ brightest point projection using x- and y-axis, separately, as the axis of rotation. Both 3D reconstructed and z-stack images were used for determining the number of GUVs with encapsulated actin bundles including those with certain structural phenotype (single ring, peripheral asters, and central asters). GUV diameters were measured by line scans from both raw actin images and GUVs. GUVs were then categorized as small (7-12 μm), medium (12-16 μm), and large (> 16 μm). The probability of the formation of an actin ring, ring/network, and network per GUV category per experiment were obtained by their count divided by the total number of captured GUVs in the specified category. The percentage of peripheral and central asters in large (or small/medium) GUVs per experiment were obtained by their count divided by the total number of captured large (or small/medium) GUVs with encapsulated actin bundles. The percentage of large (or small/medium) GUVs with actin clusters positioned at the center (or periphery) were calculated by dividing their count by the total number of large (or small/medium) GUVs with encapsulated actin bundles. GUVs encapsulating fluorescent actin monomers with no sign of bundling activity were occasionally found in each population. These GUVs were not taken into account for probability distribution and percentage measurements.

Calculation of Persistence Length

Using coordinates of the bonds and joints of each skeletonized actin bundle, MATLAB scripts were written to calculate orientational correlation function, $<C(s)> \equiv <\cos(\theta(s))>$, as a function of arc length s along the contour length of selected actin bundles. $\cos(\theta(s))$ is the cosine of the angle between snake bond vectors separated by s. $< >$ denotes ensemble average over all snake bonds as starting points. To avoid membrane curvature effect on persistence length measurement, selected actin bundles were among those with no interaction or proximity to the membrane. The lengths of selected actin bundles were $8 < L < 20$ μm.

Assuming that exponential decay of $<C(s)>$ in 3D can be described as $<C(s)> = C_0 e^{-s/L_p'}$, we fitted lines by linear regression to data points $(s, <Ln(C(s))>)$ and determined the slope $-1/L_p'$ with L_p' denoting the effective persistence length[54, 55]. Among the selected skeletonized bundles, only those with coefficient of determination $R^2 > 0.8$ were picked for persistence length measurement. Absolute value of the intercept, $Ln(|C_0|)$ for selected bundles was found to be around zero with a maximum of 0.03, underscoring the feasibility of assumption $C_0 = 1$ for persistence length measurement of actin bundles with length < 20 μm[56]. We did not find any correlation between persistence length and length of the selected actin bundles for any given experimental condition.

Statistical Analysis

Error bars in plots of experimental data represent the standard error of the mean. Probability and percentage measurements are based on 3 independent experiments. The reported p values are calculated by performing unpaired two-sample student t-tests assuming unequal variances.

Simulation Methods and Analysis

To simulate cytoskeletal networks we used the AFINES simulation package, which is described in detail elsewhere[13, 34, 35] and is summarized here. It employs a coarse-grained representation of components to simulate cytoskeletal dynamics efficiently. Specifically, filaments are modeled as worm-like chains that are represented by beads connected by springs; both the bond lengths and bond angles are subject to harmonic potentials. Similarly, crosslinkers are modeled as linear springs with sites (beads) on each end that can bind and unbind from filaments via a kinetic Monte Carlo scheme that preserves detailed balance. Molecular motors can also be described within this framework but are not included here as they are not present in the experimental system.

The positions of filaments and crosslinkers evolve by overdamped Langevin dynamics in two dimensions. Because the simulation is two-dimensional while the system of interest is not and because we expect the behavior of the experiment to be dominated be network connectivity, we

neglect excluded volume interactions between unbound components. However, crosslinker heads can bind to the same filament only if they are greater than a distance o_c μm apart, where o_c is a parameter to control the occupancy. While this may lead to quantitative artifacts in the rate of structure formation, previous work has demonstrated that this model is effective in its description of a number of *in vitro* cytoskeletal systems.

In addition to the features detailed in previous work[13, 34], we have added a circular confinement potential U^{confine} to mimic the confinement inside the GUV, and an alignment potential U^{align} between actin filaments connected by fascin or α-actinin. The potential energies of filaments (U_f) and of crosslinkers (U_{xl}) are now

$$U_f = U_f^{\text{stretch}} + U_f^{\text{bend}} + U_f^{\text{confine}} \tag{1}$$

$$U_{xl} = U_{xl}^{\text{stretch}} + U_{xl}^{\text{bind}} + U_{xl}^{\text{confine}} + U_{xl}^{\text{align}} \tag{2}$$

For brevity we only describe the added terms. The confinement potential U^{confine} is implemented as a radial confinement potential starting at radius r_c with a tunable force constant k_c,

$$U^{\text{confine}} = \begin{cases} \frac{1}{2} k_c (r - r_c)^2 & if\ r \geq r_c \\ 0 & if\ r < r_c \end{cases} \tag{3}$$

where r is the distance of the filament or crosslinker bead from the origin.

For α-actinin we set $U_{xl}^{\text{align}} = 0$. For fascin,

$$U_{xl}^{\text{align}} = k_{xl}^{\text{align}}(1 - \cos\theta) \tag{4}$$

where k_{xl}^{align} is the penalty parameter for the angle θ between the springs of the bound filaments. This term penalizes binding to filaments that are not parallel. The penalty parameter for fascin was set to $k_{xl}^{\text{align}} = \frac{1}{3}\ pN \cdot \mu m$, while the penalty was not implemented for α-actinin.

14

We utilize these new features and the existing functionality of the AFINES package to model α-actinin and fascin. One chief difference between the two crosslinkers is their respective lengths, with fascin being almost a factor of 6 smaller[11]. As such, fascin is represented as short, $\ell = 0.1\ \mu m$, and stiff, $\kappa = 1\ pN/\mu m$, while α-actinin is relatively long, $\ell = 0.5\ \mu m$, and soft, $\kappa = 0.1\ pN/\mu m$. Sizes larger than the experimental structures are needed to compensate for the fact that the springs in the simulation are softer than individual proteins, as discussed previously[13]. That fascin bundles only parallel filaments and α-actinin has no preference between parallel and anti-parallel filaments was captured through the U_{xl}^{align} potential, as described above. The simulation parameters are summarized in **Table S1**.

The initial condition of the simulation was generated by first creating each 35-bead filament centered on the origin. After creation, the segment connecting the center to the pointed end was rotated by a random angle drawn uniformly from 0 to 2π. The angle of the other half of the filament was obtained by adding an angle uniformly drawn from between $-\frac{\pi}{4}$ and $\frac{\pi}{4}$ and adding this angle to that of the first segment. Thus, each filament was assigned some random initial bend. Once the angles were assigned, the filament center was moved off of the origin by translating the bead positions in x and y. The amount of displacement in each direction was drawn from a gaussian distribution centered at 0 with a standard deviation of 3 μm. Crosslinker initial positions were drawn with uniform probability from the box centered on the origin with dimensions $r_c \times r_c$ where r_c is the radius of the confining circle, which in these simulations is 15 μm. Both crosslinkers are simulated at a density of 5 μm^{-2} within the vesicle. Each simulation ran for 100 s with a time step of 2×10^{-5} s. The updated version of AFINES including the new features described here as well as the full configuration files used to run these simulations and the script used to generate the initial conditions are available at https://github.com/Chatipat-and-Steven-friendship-forever/AFINES/tree/chatipat_integrate/crosslinker_sorting_in_GUVs. The parameters of the simulation box and actin can be found in **Table S2**.

To characterize the spatial distribution of crosslinkers at a given time, we construct a list of all of the Cartesian coordinates of crosslinkers for which both heads are bound to filaments in that frame. From this list we compute a two-dimensional histogram of crosslinker locations with 20 bins in each dimension. This histogram is normalized by dividing the value of each bin by the area of the bin and the total number of crosslinkers considered. In this manner, we turn our

histogram into a probability density function (PDF) that is normalized to one. The images shown in **Fig. 4f** are averages over the PDFs for the final frames of five independent simulations.

We also compute the Binder cumulant, a measure of the kurtosis of the distribution. This measure is frequently used in statistical physics to determine phase transition points in numerical simulations, and is given by

$$U_4 = 1 - \frac{\langle s^4 \rangle}{3 \langle s^2 \rangle^2} \tag{5}$$

where s is an order parameter. In our case, s is the value at one point of a crosslinker PDF for an individual simulation, and $\langle \ \ \rangle$ denotes a spatial average. The lines shown in **Fig. 4g** are averages over five independent simulations, and the error bars indicate one standard deviation from these averages.

Author Contributions

YB and APL designed the experiments. YB conducted the experiments and analyzed the experimental data. AG, YB, and APL prepared purified proteins. YB, TL, and PS developed the image analysis methods. ARD, GMH, SAR, and CL designed the modeling and simulations. SAR and CL performed and analyzed the simulations. YB, APL, SAR, GMH, and ARD wrote the manuscript. All authors discussed the results and commented on the manuscript.

Acknowledgements

Competing Interests

The authors declare no competing interests.

Figure Captions:

Figure 1. GUV size- and crosslinker concentration-dependent organization of actin-α-actinin networks. a, Representative 3D reconstructed fluorescence confocal images of actin networks of different α-actinin:actin ratios (actin concentration at 5 µM). Actin bundles form networks in larger GUVs, while they form single rings in smaller GUVs. Dotted lines outline GUV boundaries. Scale bar, 10 µm. **b,** Cumulative probability (for all 3 α-actinin concentrations) of ring and network formation in GUVs with different sizes. **c, d,** Probability of the formation of rings and networks at different α-actinin concentrations. Error bars indicate standard error of the mean; n = 3 experiments. N_{GUVs} per experiment = [389 42 23], [67 45 38], [188 145 128] in order of ascending α-actinin concentration (numbers in brackets are arranged in order of ascending GUV diameter). *p* values compare formation probabilities of rings (c) and networks (d) in small and large GUVs. **e,** Representative 3D reconstructed image from confocal stack of fluorescence images of an encapsulated α-actinin/actin (3:10 [M/M]) network. High α-actinin concentration can induce the formation of dense clusters at the GUV periphery. Scale bar, 10 µm. **f,** The probability of the formation of actin peripheral asters depends on GUV size. The majority of actin bundles form peripheral asters in larger GUVs. Error bars indicate standard error of the mean; n = 3 experiments. N_{GUVs} per experiment = [429 23], [112 38], [333 128] in order of ascending α-actinin concentration (numbers in brackets are arranged in order of ascending GUV diameter). *p* values compare peripheral aster formation probabilities for the two ranges of GUV diameters. **g,** Cumulative (3 experiments) proportion of peripheral asters with peripheral bundles (all actin bundles elongated around GUV periphery) and lumenal bundles (with at least one actin bundle elongated in GUV lumen) in large GUVs (diameter > 16 µm). At high α-actinin concentrations, the majority of actin bundles form asters with all actin bundles elongated around the periphery (peripheral bundles). Number of large GUVs with peripheral asters = [35, 14, 53] in order of ascending α-actinin concentration. **h,** Schematic summarizing the result of encapsulated actin network assembly by α-actinin (without fascin) in different sized vesicles. Blue arrows show the merging of actin filament bundles (green dashed lines) into distinct peripheral bundles (green solid lines).

Figure 2. GUV size-dependent formation of rings, peripheral asters, and central asters by α-actinin and fascin. a, Representative 3D-reconstructed (left) and skeletonized (right) images from

a confocal fluorescence image stack of 5 µM actin (10% ATTO 488 actin) bundled by 0.5 µM fascin and 1 µM α-actinin in GUVs (composition: 69.9% DOPC, 30% cholesterol, and 0.1% rhodamine-PE). Yellow arrow denotes a cluster of actin fluorescence in a central aster. White arrows denote clusters of actin fluorescence in peripheral asters. Color in the skeletonized image shows z position. Scale bar, 10 µm. **b,** Cumulative probability (α-actinin concentrations of 0.5, 1, and 1.5 µM with 0.5 µM fascin and 5 µM actin) of ring and network formation in GUVs with different sizes. **c,** Schematic representation of GUV-size dependent actin networks assembled by α-actinin and fascin. Rings and peripheral asters can occasionally deform GUVs. **d, e,** Probability of the formation of rings **(d)** and networks **(e)** at different α-actinin concentrations as a function of GUV diameter. N_{GUVs} per experiment = [101 98 29], [147 58 71], [137 82 24] in order of ascending α-actinin concentration (numbers in brackets are arranged in order of ascending GUV diameter). *p* values compare formation probabilities of rings (c) and networks (d) in small and large GUVs. **f,** Probability of aster formation (peripheral or central) in the presence of fascin and α-actinin. Aster formation depends on GUV size but not α-actinin concentration. Fascin/actin, 0.1 (M/M). All error bars indicate standard error of the mean; n = 3 experiments. N_{GUVs} per experiment = [199 29], [205 71], [219 24] in order of ascending α-actinin concentration (numbers in brackets are arranged in order of ascending GUV diameter). *p* values compare aster formation probabilities in the two ranges of GUV diameters.

Figure 3. Flexural rigidity of actin bundles and GUV-size dependent localization of F-actin clusters in the presence of α-actinin and fascin suggests crosslinker sorting and domain formation. a, Representative 2D (left) confocal fluorescence images of actin networks shown by arrows (3D reconstructed image, middle) along with skeletonized (right) image of the GUV populations. α-actinin, 0.5 µM (top), 1.5 µM (bottom). Fascin, 0.5 µM. Actin, 5 µM. Scale bar, 10 µm. **b,** Actin fluorescence intensity along the length of dashed lines drawn across the two GUVs in (a) normalized to the GUV diameters. **c,** Cumulative probability (for all α-actinin concentrations) of the aggregation of crosslinked actin with/without fascin in GUVs with diameter > 20 µm. α-actinin-fascin-actin bundles tend to shift cluster localization from the periphery to the center of GUVs. Probabilities do not add to 100% because a portion of actin bundles do not cluster at either the center or the periphery. $N_{GUVs>20\ \mu m}$ = 167 [87 (α-actinin), 80 (α-actinin+fascin)]. In

our analysis, only a minority of vesicles with encapsulated α-actinin-actin bundle structures and encapsulated α-actinin-fascin-actin bundle structures did not form clusters. **d**, Cumulative probability (for all α-actinin concentrations) of the aggregation of crosslinked actin in large GUVs in the presence of both α-actinin and fascin. Larger GUVs facilitate centering of clusters. A portion of actin bundles do not cluster either at the center or at the periphery. $N_{analyzed\ GUVs>16\ \mu m}$ = 87 (61 [17-24 μm], 26 [>24 μm]).

Figure 4. α-actinin and fascin sort in central aster structures. a, Representative 3D reconstructed confocal fluorescence images of α-actinin, actin, merged, and skeletonized construct of an encapsulated central aster respectively, from left to right. α-actinin, 1.5 μM. Fascin, 0.5 μM. Actin, 5 μM. Scale bar, 10 μm. **b, c,** Fluorescence intensity of α-actinin and actin along the dashed line drawn across the GUV **(b)** and circle drawn around central aster outside the actin cluster **(c)** in (a). **d,** Persistence length of actin bundles without and with fascin (fascin/actin, 0.1 [M/M]) at different α-actinin/actin ratios indicated. L_p [fascin:α-actinin:actin] = 33.3 ± 10 μm [0:1:10], 39.3 ± 9 μm [0:3:10], 54.2 ± 11.4 μm [1:1:10], and [1:1:10], 77.8 ± 19 μm [1:2:10], and 99.7 ± 15 μm [1:3:10]). $N_{bundles}$ = [22 14 17 14 26] in order of *x*-axis categories; 3 GUVs per category. **e,** Representative structure after 100 s of simulation of actin filaments (red) crosslinked by α-actinin (cyan) and fascin (black). The border of the containing circle is shown in black. **f,** PDFs of α-actinin (left) and fascin (right) from either simulation of each alone with actin (top row) or the two in combination with actin (bottom row). PDFs are constructed from the last frames of five independent simulations of 100 s for each condition. **g,** Binder cumulant as a function of time for each crosslinker separately with actin (top) and the combined simulation (bottom). Values are measured for each simulation independently and then averaged. Error bars represent one standard deviation from the mean. **h**, Schematic of crosslinker size-dependent sorting in confined α-actinin-fascin crosslinked actin network.

References

1.   Pegoraro AF, Janmey P, Weitz DA. Mechanical properties of the cytoskeleton and cells. *Cold Spring Harb Perspect Biol* 2017, **9**(11)**:** a022038.

2.   Fletcher DA, Mullins RD. Cell mechanics and the cytoskeleton. *Nature* 2010, **463**(7280)**:** 485-492.

3.   Blanchoin L, Boujemaa-Paterski R, Sykes C, Plastino J. Actin dynamics, architecture, and mechanics in cell motility. *Physiol Rev* 2014, **94**(1)**:** 235-263.

4.   Dumont S, Prakash M. Emergent mechanics of biological structures. *Mol Biol Cell* 2014, **25**(22)**:** 3461-3465.

5.   Luo T, Mohan K, Iglesias PA, Robinson DN. Molecular mechanisms of cellular mechanosensing. *Nat Mater* 2013, **12**(11)**:** 1064-1071.

6.   Vignaud T, Copos C, Leterrier C, Toro-Nahuelpan M, Tseng Q, Mahamid J*, et al.* Stress fibres are embedded in a contractile cortical network. *Nat Mater* 2020**:** 1-11.

7.   Jacquemet G, Hamidi H, Ivaska J. Filopodia in cell adhesion, 3D migration and cancer cell invasion. *Curr Opin Cell Biol* 2015, **36:** 23-31.

8.   Vignjevic D, Yarar D, Welch MD, Peloquin J, Svitkina T, Borisy GG. Formation of filopodia-like bundles in vitro from a dendritic network. *J Cell Biol* 2003, **160**(6)**:** 951-962.

9.   Brieher WM, Coughlin M, Mitchison TJ. Fascin-mediated propulsion of Listeria monocytogenes independent of frequent nucleation by the Arp2/3 complex. *J Cell Biol* 2004, **165**(2)**:** 233-242.

10.   Tseng Y, Kole TP, Lee JS, Fedorov E, Almo SC, Schafer BW*, et al.* How actin crosslinking and bundling proteins cooperate to generate an enhanced cell mechanical response. *Biochem Biophys Res Commun* 2005, **334**(1)**:** 183-192.

11.   Winkelman JD, Suarez C, Hocky GM, Harker AJ, Morganthaler AN, Christensen JR*, et al.* Fascin- and α-actinin-bundled networks contain intrinsic structural features that drive protein sorting. *Curr Biol* 2016, **26**(20)**:** 2697-2706.

12.   Kadzik RS, Homa KE, Kovar DR. F-Actin Cytoskeleton Network Self-Organization Through Competition and Cooperation. *Annu Rev Cell Dev Biol* 2020, **36:** 35-60.

13.   Freedman SL, Suarez C, Winkelman JD, Kovar DR, Voth GA, Dinner AR*, et al.* Mechanical and kinetic factors drive sorting of F-actin cross-linkers on bundles. *Proc Natl Acad Sci U S A* 2019, **116**(33)**:** 16192-16197.

14.   Qiu Y, Nguyen M, Hocky GM, Dinner AR, Vaikuntanathan S. A strong non-equilibrium bound for sorting of crosslinkers on growing biopolymers. *arXiv preprint arXiv:201211588* 2020.

15.   Co C, Wong DT, Gierke S, Chang V, Taunton J. Mechanism of actin network attachment to moving membranes: barbed end capture by N-WASP WH2 domains. *Cell* 2007, **128**(5)**:** 901-913.

16.   Ganzinger KA, Vogel SK, Mücksch J, Blumhardt P, Schwille P. Myosin-II activity generates a dynamic steady state with continuous actin turnover in a minimal actin cortex. *J Cell Sci* 2019, **132**(4).

17.   Köster DV, Husain K, Iljazi E, Bhat A, Bieling P, Mullins RD*, et al.* Actomyosin dynamics drive local membrane component organization in an in vitro active composite layer. *Proc Natl Acad Sci U S A* 2016, **113**(12)**:** E1645-E1654.

18.   Liu AP, Fletcher DA. Actin polymerization serves as a membrane domain switch in model lipid bilayers. *Biophys J* 2006, **91**(11)**:** 4064-4070.

19.   Liu AP, Richmond DL, Maibaum L, Pronk S, Geissler PL, Fletcher DA. Membrane-induced bundling of actin filaments. *Nat Phys* 2008, **4**(10)**:** 789-793.

20.   Simon C, Kusters R, Caorsi V, Allard A, Abou-Ghali M, Manzi J*, et al.* Actin dynamics drive cell-like membrane deformation. *Nat Phys* 2019, **15**(6)**:** 602-609.

21.   Malik-Garbi M, Ierushalmi N, Jansen S, Abu-Shah E, Goode BL, Mogilner A*, et al.* Scaling behaviour in steady-state contracting actomyosin networks. *Nat Phys* 2019, **15**(5)**:** 509-516.

22.   Vogel SK, Wolfer C, Ramirez-Diaz DA, Flassig RJ, Sundmacher K, Schwille P. Symmetry Breaking and Emergence of Directional Flows in Minimal Actomyosin Cortices. *Cells* 2020, **9**(6)**:** 1432.

23.   Bashirzadeh Y, Liu AP. Encapsulation of the cytoskeleton: towards mimicking the mechanics of a cell. *Soft Matter* 2019, **15**(42)**:** 8425-8436.

24.   Lee KY, Park SJ, Lee KA, Kim SH, Kim H, Meroz Y*, et al.* Photosynthetic artificial organelles sustain and control ATP-dependent reactions in a protocellular system. *Nat Biotechnol* 2018, **36**(6)**:** 530-535.
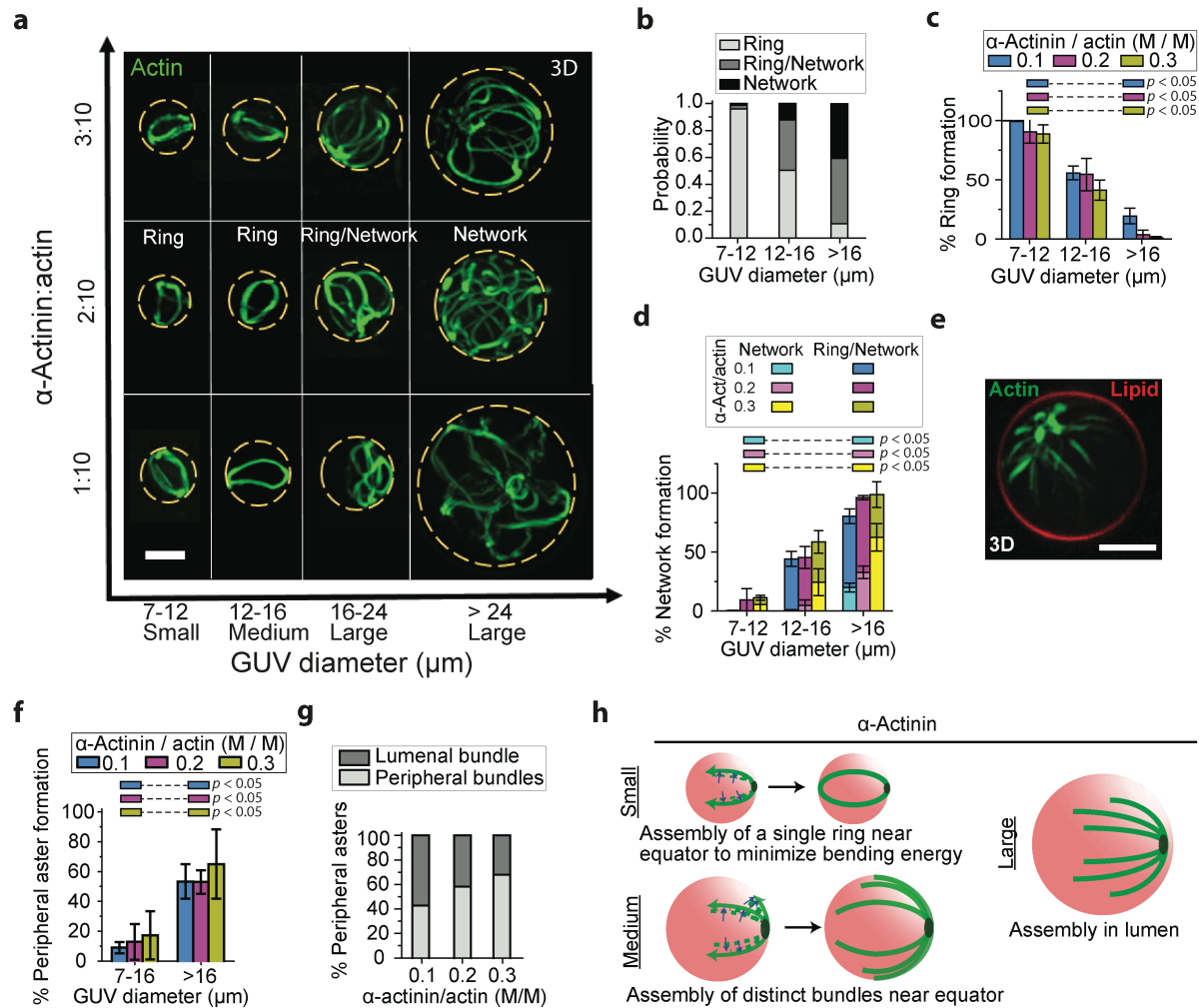
25.   Liu AP, Fletcher DA. Biology under construction: in vitro reconstitution of cellular function. *Nat Rev Mol Cell Biol* 2009, **10**(9)**:** 644-650.

26.   Kelley CF, Litschel T, Schumacher S, Dedden D, Schwille P, Mizuno N. Phosphoinositides regulate force-independent interactions between talin, vinculin, and actin. *Elife* 2020, **9:** e56110.

27.   Baumann H, Surrey T. Motor-mediated cortical versus astral microtubule organization in lipid-monolayered droplets. *J Biol Chem* 2014, **289**(32)**:** 22524-22535.

28.   Colin A, Singaravelu P, Thery M, Blanchoin L, Gueroui Z. Actin-Network Architecture Regulates Microtubule Dynamics. *Curr Biol* 2018, **28**(16)**:** 2647-2656 e2644.

29.   Good MC, Vahey MD, Skandarajah A, Fletcher DA, Heald R. Cytoplasmic volume modulates spindle size during embryogenesis. *Science* 2013, **342**(6160)**:** 856-860.

30.   Litschel T, Kelley CF, Holz D, Koudehi MA, Vogel SK, Burbaum L*, et al.* Reconstitution of contractile actomyosin rings in vesicles. *bioRxiv* 2020**:** 2020.2006.2030.180901.

31.   Miyazaki M, Chiba M, Eguchi H, Ohki T, Ishiwata S. Cell-sized spherical confinement induces the spontaneous formation of contractile actomyosin rings in vitro. *Nat Cell Biol* 2015, **17**(4)**:** 480-489.

32.   Bashirzadeh Y, Wubshet NH, Liu AP. Confinement Geometry Tunes Fascin-Actin Bundle Structures and Consequently the Shape of a Lipid Bilayer Vesicle. *Front Mol Biosci* 2020, **7**(337)**:** 610277.

33.   Haviv L, Brill-Karniely Y, Mahaffy R, Backouche F, Ben-Shaul A, Pollard TD*, et al.* Reconstitution of the transition from lamellipodium to filopodium in a membrane-free system. *Proc Natl Acad Sci U S A* 2006, **103**(13)**:** 4906-4911.

34.   Freedman SL, Banerjee S, Hocky GM, Dinner AR. A Versatile Framework for Simulating the Dynamic Mechanical Structure of Cytoskeletal Networks. *Biophys J* 2017, **113**(2)**:** 448-460.

35.   Freedman SL, Hocky GM, Banerjee S, Dinner AR. Nonequilibrium phase diagrams for actomyosin networks. *Soft Matter* 2018, **14**(37)**:** 7740-7747.

36.   Nedelec F, Foethke D. Collective Langevin dynamics of flexible cytoskeletal fibers. *NJPh* 2007, **9**(11)**:** 427.

37.   Koenderink GH, Paluch EK. Architecture shapes contractility in actomyosin networks. *Curr Opin Cell Biol* 2018, **50:** 79-85.

38. e Silva MS, Depken M, Stuhrmann B, Korsten M, MacKintosh FC, Koenderink GH. Active multistage coarsening of actin networks driven by myosin motors. *Proc Natl Acad Sci U S A* 2011, **108**(23)**:** 9408-9413.

39. Ierushalmi N, Malik-Garbi M, Manhart A, Abu Shah E, Goode BL, Mogilner A*, et al.* Centering and symmetry breaking in confined contracting actomyosin networks. *Elife* 2020, **9:** e55368.

40. Adeli Koudehi M, Rutkowski DM, Vavylonis D. Organization of associating or crosslinked actin filaments in confinement. *Cytoskeleton (Hoboken)* 2019, **76**(11-12)**:** 532-548.

41. Pelletier O, Pokidysheva E, Hirst LS, Bouxsein N, Li Y, Safinya CR. Structure of actin cross-linked with alpha-actinin: a network of bundles. *Phys Rev Lett* 2003, **91**(14)**:** 148102.

42. Lieleg O, Schmoller KM, Cyron CJ, Luan Y, Wall WA, Bausch AR. Structural polymorphism in heterogeneous cytoskeletal networks. *Soft Matter* 2009, **5**(9)**:** 1796-1803.

43. Tempel M, Isenberg G, Sackmann E. Temperature-induced sol-gel transition and microgel formation in alpha -actinin cross-linked actin networks: A rheological study. *Phys Rev E Stat Phys Plasmas Fluids Relat Interdiscip Topics* 1996, **54**(2)**:** 1802-1810.

44. Svitkina TM, Bulanova EA, Chaga OY, Vignjevic DM, Kojima S-i, Vasiliev JM*, et al.* Mechanism of filopodia initiation by reorganization of a dendritic network. *J Cell Biol* 2003, **160**(3)**:** 409-421.

45. Schmid EM, Bakalar MH, Choudhuri K, Weichsel J, Ann HS, Geissler PL*, et al.* Size-dependent protein segregation at membrane interfaces. *Nat Phys* 2016, **12**(7)**:** 704-711.

46. James JR, Vale RD. Biophysical mechanism of T-cell receptor triggering in a reconstituted system. *Nature* 2012, **487**(7405)**:** 64-69.

47. Pardee JD, Aspudich J. [18] Purification of muscle actin. *Meth. Enzymol*, vol. 85. Elsevier, 1982, pp 164-181.

48. Abkarian M, Loiseau E, Massiera G. Continuous droplet interface crossing encapsulation (cDICE) for high throughput monodisperse vesicle design. *Soft Matter* 2011, **7**(10)**:** 4610-4614.

49. Schneider CA, Rasband WS, Eliceiri KW. NIH Image to ImageJ: 25 years of image analysis. *Nat Methods* 2012, **9**(7)**:** 671-675.

50. Schindelin J, Arganda-Carreras I, Frise E, Kaynig V, Longair M, Pietzsch T*, et al.* Fiji: an open-source platform for biological-image analysis. *Nat Methods* 2012, **9**(7)**:** 676-682.
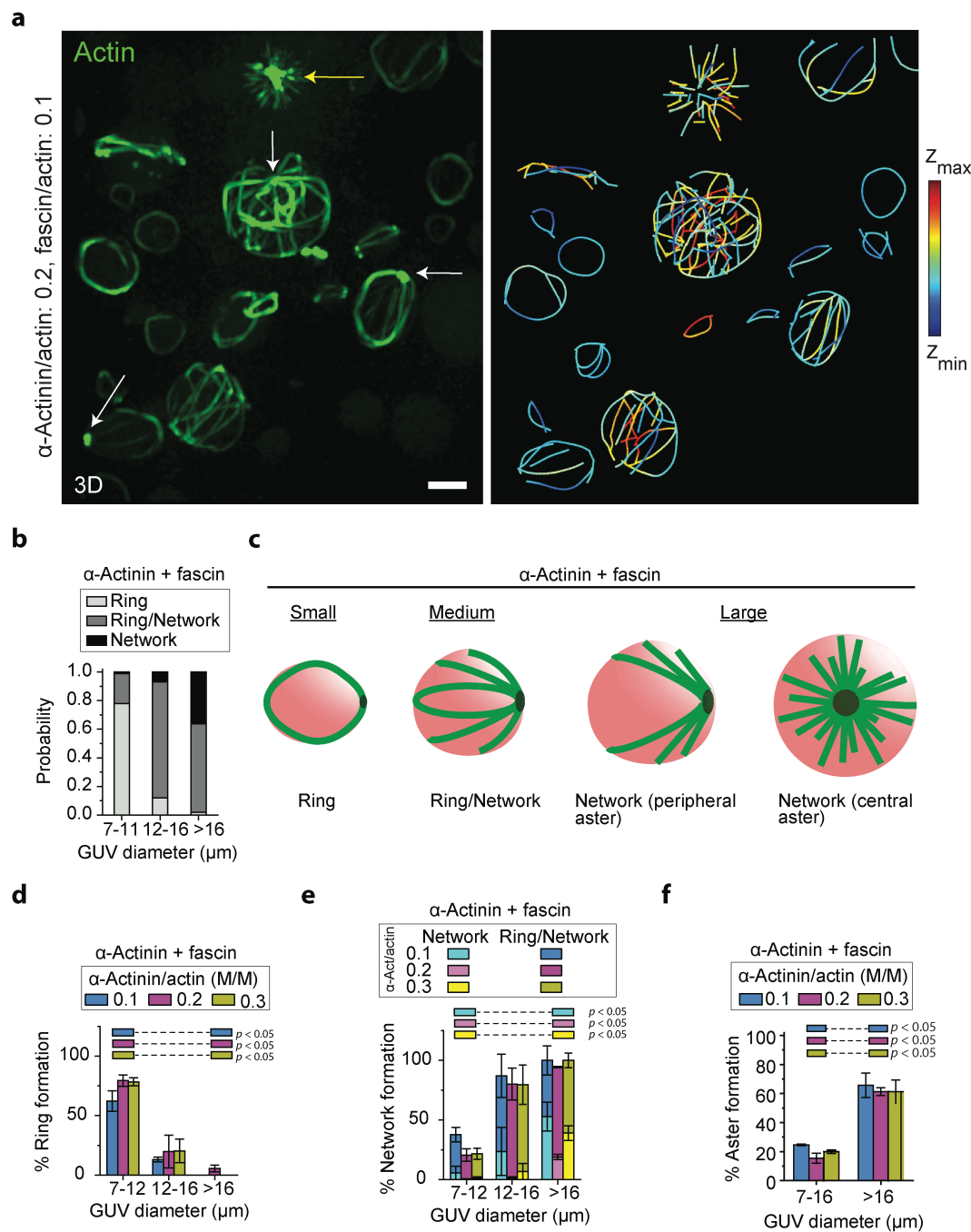
51.   Xu T, Vavylonis D, Huang X. 3D actin network centerline extraction with multiple active contours. *Med Image Anal* 2014, **18**(2)**:** 272-284.

52.   Xu T, Vavylonis D, Tsai FC, Koenderink GH, Nie W, Yusuf E*, et al.* SOAX: a software for quantification of 3D biopolymer networks. *Sci Rep* 2015, **5**(1)**:** 9081.

53.   Pettersen EF, Goddard TD, Huang CC, Couch GS, Greenblatt DM, Meng EC*, et al.* UCSF Chimera--a visualization system for exploratory research and analysis. *J Comput Chem* 2004, **25**(13)**:** 1605-1612.

54.   Hsu H-P, Paul W, Binder K. Standard definitions of persistence length do not describe the local "intrinsic" stiffness of real polymer chains. *Macromolecules* 2010, **43**(6)**:** 3094-3102.

55.   Ullner M, Woodward CE. Orientational correlation function and persistence lengths of flexible polyelectrolytes. *Macromolecules* 2002, **35**(4)**:** 1437-1445.

56.   Takatsuki H, Bengtsson E, Mansson A. Persistence length of fascin-cross-linked actin filament bundles in solution and the in vitro motility assay. *Biochim Biophys Acta* 2014, **1840**(6)**:** 1933-1942.
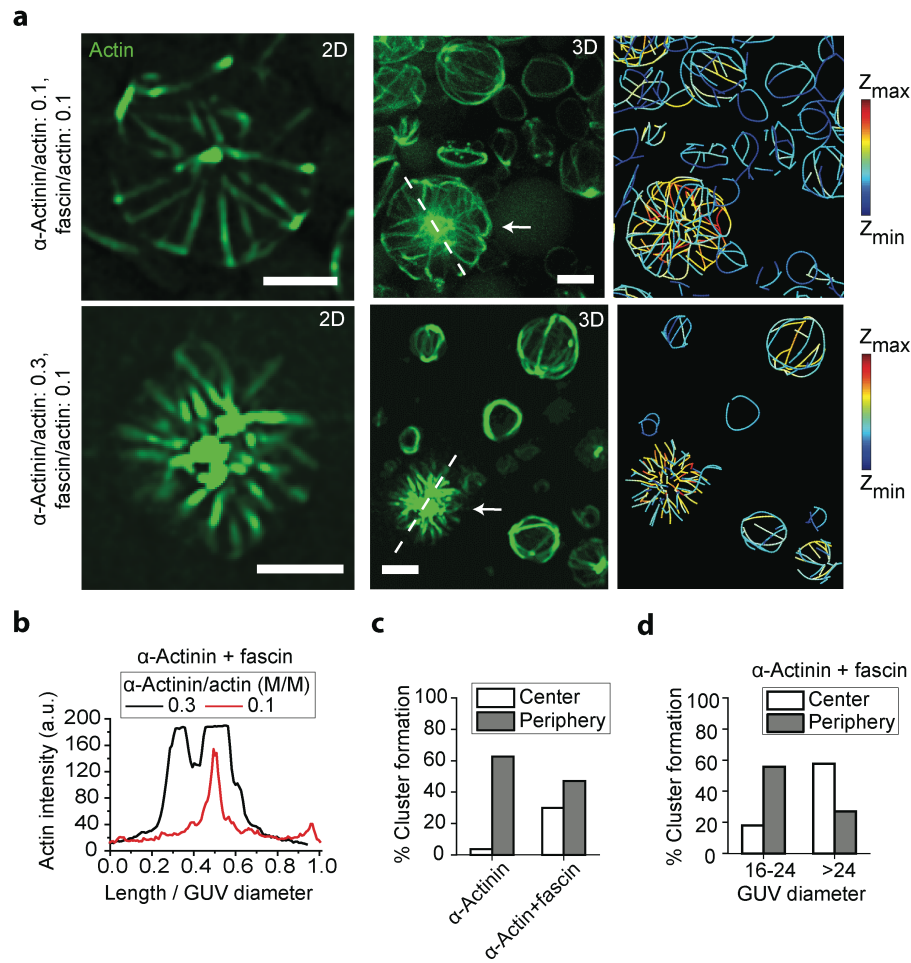
Figure 1

Figure 2

Figure 3

Figure 4